

# Coarse-Grained Simulation of Surfactant Membrane

Hayato SHIBA and Hiroshi NOGUCHI

*Institute for Solid State Physics, University of Tokyo*

*Kashiwa-no-ha, Kashiwa, Chiba 277-8581*

## Abstract

We review our recent studies on the structure formation of surfactant membranes using a meshless membrane model, in which a unit particle represent a patch of the bilayer membrane. We revealed aggregation of ligand–receptor sites binding neighboring membranes, microdomain formation induced by grafted polymer chains, and the formation of a rolled lamellar structure under shear flow using massive parallel simulations.

## 1 Introduction

Amphiphilic molecules, such as lipids and detergents, self-assemble into various structures such as micelles and bilayer membranes, which display a rich variety of rheological properties under flow. In particular, the bilayer membrane is the basic structure of the plasma membrane and intracellular compartments of living cells, where the membranes are in a fluid phase and lipid molecules can diffuse in two-dimensional space.

Cell adhesion is a fundamental process required for the removal of foreign bodies in immune response and for cell motility. It is mediated by specific (ligand–receptor) and non-specific interactions. Recently, lateral interactions between ligand–receptor binding sites in membranes have been received growing attention [1, 2]. The cooperative aggregation of the adhesion sites yields various patterns of adhesion domains and also morphological changes

in cells and liposomes.

The membrane height fluctuations yield a repulsive force  $f \sim d^{-3}$  between tensionless fluid membranes with a neighboring membrane distance  $d$ . Since the adhesion bond holds two membranes close to each other, an effective attraction works between the adhesion sites. If the adhesion sites are aggregated, the rest of the regions of the membranes are allowed to have large height fluctuations. This entropy gain yields an attraction between adhesion sites. Several groups have been investigated this entropic interaction theoretically and via simulations. These studies have reported a weak attraction between adhesion sites, which induces small temporal clusters. However, it has been concluded that this force is too weak to form a large cluster by itself, and thus, the researchers have included additional pairwise interactions to investigate the phase separation. Using ISSP super computer system B, we have clarified the condition that induces aggregation of the adhesion sites purely by entropic interactions [3].

in living cells, it is considered that local microdomains, called lipid rafts, are formed on biomembranes as a platform of many biological functions. Lipid rafts is in diameter of  $10 \sim 100$  nm, and proteins, cholesterol, and glycosphingolipids are concentrated. We have investigated the membranes with grafted polymer chain such as glycolipids and PEG-conjugated lipids [4]. We found that the polymer grafting can reduce the line tension of the

membrane edges and membrane domains and stabilize small domains.

About 20 years ago, a salient phenomenon has been found in surfactant systems. Applying shear flow to dilute lamellar phases in surfactant-water mixtures in a Couette cell, the found formation of densely packed multilamellar vesicles like onion [5]. Each onion represents a unit cell of the periodic structure and its layer number is larger than a hundred. Although there have been numerous efforts to understand the onion formation mechanism, the problem was revealed to be too difficult for theoretical analysis. Only very recently, a non-equilibrium free energy analysis has revealed the stability of densely packed lamellar under shear flow more than a little [6].

The transition path and dynamics of transition is still under debate. Scattering experiments (SAXS and SANS) has been conducted under shear flow, and a concentric pattern formation of multilamellar layers has been observed as a precursor state of the onion state [7]. Because this structure has  $\mu\text{m}$  scale structure, electric microscope image cannot capture the arrangement of the layers, and thus, how the structure is arranged is not completely understood. We tackled this problem using massive parallel simulations of a highly coarse-grained membrane model [8, 9].

## 2 Model

Coarse-grained models pave the way to simulate large molecular assemblies as typified by soft matter including biomembranes, colloids, liquid crystals, and so on. Various coarse-grained models have been developed to simulate a membrane as an assembly of surfactant molecules [10]. Coarse-grained lipid molecules have been proposed with explicit and implicit solvent. A coarse-grained molecular simulation can only reach lamellar phase with around 10 layers with typical computational power [11], and thus, we need a different approach to enter

into investigation of collective instability represented in the experiments mentioned above.

Our basic approach is to adopt a model highly coarse-grained to tens of nm scales and realize a large scale simulation to enable numerical analysis of mm scale systems. The model employed in this study is one of the meshless membrane model [12], in which coarse-grained particles self-assemble into a single layer membrane. Because this model is particle-based, the membranes not only deform but also can exhibit topological changes including rupture and reconnection, and thus, dynamics induced by topological defects their time development can be studied with this model.

The interaction potential of the model is given by

$$\frac{U}{k_B T} = \sum_{i < j} U_{\text{rep}} + \sum_i (\epsilon U_{\text{att}} + k_\alpha \alpha_{\text{pl}}) \quad (1)$$

In Eq. (1), The first term  $U_{\text{rep}}$  represents short-ranged repulsive interaction energy, which results in two-body forces between all the nearest neighbor pairs. The second term consists of multibody attractive interaction and curvature potential giving rise to bending rigidity: the former attractive interaction is represented using the local density  $\rho_i = \sum_j f_{\text{cut}}(r_{ij}/\sigma)$

$$U_{\text{att}} = 0.25 \ln\{1 + \exp[-4(\rho_i - \rho^*)]\} - C. \quad (2)$$

$f_{\text{cut}}$  is a cutoff function satisfying  $C^\infty$  continuity defined as

$$f_{\text{cut}}(s) = \exp \left[ a \left( 1 + \frac{1}{(|s|/s_{\text{cut}})^n - 1} \right) \right]. \quad (3)$$

when  $s$  is smaller than a cutoff distance  $s_{\text{cut}}$  and otherwise  $f_{\text{cut}}(s) = 0$ .  $\rho^*$  is optimal local density which is set to 6 in this paper. This potential is a multibody potential and gives rise to attractive interaction between  $i$  and others only when the local density is low enough *i.e.*  $\rho_i < \rho^*$

The latter term in the 2nd term in Eq. (1) is defined so that it is proportional to “aplanarity”  $\alpha_{\text{pl}}$ .  $\alpha_{\text{pl}}$  is defined so that it is proportional to local degree of deviation from a planar shape around each particle, using the eigenvalues  $\lambda_1, \lambda_2, \lambda_3$  of local gyration tensor

$$\alpha_{\text{pl}} = \frac{9\lambda_1\lambda_2\lambda_3}{(\lambda_1 + \lambda_2 + \lambda_3)(\lambda_1\lambda_2 + \lambda_2\lambda_3 + \lambda_3\lambda_1)} \quad (4)$$

When particles are aligned in a planar shape with curvature, the minimum eigenvalue assumes a very small value ( $\lambda_1 \ll \lambda_2, \lambda_3$ ). The minimum eigenvalue corresponds to the deviation from the planar shape, see Ref. [12] for a detailed explanation. Since the representation of Eq. (4) is symmetric with respect to the three eigenvalues,  $\alpha_{\text{pl}}$  can be easily deduced from three invariants of the gyration tensors of surrounding particles without calculating the eigenvalues.

To simulate the membranes with ligand–receptor adhesion sites and grafted polymers, solvent-free membranes are employed, where solvent effects are implicitly treated as an effective attractive interactions between membrane particles.

To simulate structure formation of multilamellar layers, we extended the meshless membrane model into explicit solvent simulation. Solvent particles interact with other solvent and membrane particles via the repulsive interaction  $U_{\text{rep}} = \sum_{i < j} (\sigma_{ij}/r_{ij})^{12}$ . The system is then composed of membrane ( $\mathcal{A}$ ) and solvent ( $\mathcal{B}$ ) particles. The total number density of the particles fixed at  $\phi = N/V = 0.64\sigma^{-3}$ , where the total number of the particles  $N = N_{\mathcal{A}} + N_{\mathcal{B}} = 960000$ . In the following, the composition (almost equal to the volume fraction) of the membrane particles will be denoted as  $\varphi = N_{\mathcal{A}}/N$ .

### 3 Simulation method

The above model is simulated in an NVT ensemble. To keep the temperature constant, the

equation of motion of the particles are solved using a Langevin thermostat for solvent-free model and a dissipative particle dynamics thermostat for an explicit-solvent model. In the dissipative particle dynamics, a Langevin thermostat is applied to the relative velocities between all the neighbor particle pairs, conserving the momentum to produce hydrodynamics of the solvent.

In the simulations under shear flow, the parallel simulation runs using 256 CPUs (1024 cores) has been conducted on the System B. The parallelization has been coded using the spacial decomposition, and the code has been developed from scratch by the first author. In this parallelization, the total simulation volume is separated into MPI boxes corresponding to rectangular boxes. In each box, the positions and velocities of particles on the edge is transferred to and from its neighboring boxes, as with the usual parallel molecular dynamics scheme (See Fig. 1 (a) for schematic image).<sup>7</sup> The main features of this code is the following.

#### 1. Hybrid parallelization

Each MPI process box are further divided into smaller cells which are used for searching neighbor particle pairs. In calculating the force for each particle  $\mathbf{f}_i$ , the force is accumulated pair by pair, to reduce the total calculation amount.

$$\mathbf{f}_i^x += \mathbf{f}_{ij}^x = \frac{\partial U}{\partial x_{ij}}, \quad \mathbf{f}_j^x += -\mathbf{f}_{ij}^x \quad (5)$$

Here,  $x_{ij} = x_i - x_j$  and the same pairwise interaction force  $\mathbf{f}_{ij}^x$  is used for particles  $i$  and  $j$ . OpenMP thread parallelization of such an arithmetic cannot be implemented in a simple manner, because multiple access to the same memory address for  $\mathbf{f}_x^i$  can happen. To avoid this, we divided separated cells into the same group, and distributed force-update processing for separated cells to different OpenMP threads.

#### 2. Lees-Edwards boundary condition

To yield the shear flow, Lees-Edwards (LE) boundary condition is adopted. LE boundary condition is a sort of skewed periodic boundary condition, in which particles go out of the periodic walls in the shear gradient direction (parallel to  $z$ -axis), the velocity and the coordinate of the particles are changed as follows:

$$\begin{cases} v_x^{\text{top}} = v_x^{\text{bottom}} + \dot{\gamma}L_z \\ x^{\text{top}} = x^{\text{bottom}} + \dot{\gamma}L_z t \end{cases} \quad (6)$$

“top” and “bottom” indicate that the positions of the particles on the boundary at  $z = L_z/2$  and  $-L_z/2$ , respectively.

To keep MPI parallelization efficiency, combinations of neighbor MPI box pairs should be kept, because communication with many far-away processes drag down the simulation speed. In our simulation, the neighbor box pairs between the top and bottom parts are kept by deforming the whole MPI process box and the cells together. When the strain reaches 0.5 *i.e.* its inclination becomes 45-degree, the whole system is converted to the equivalent state with strain  $-0.5$ , using all-to-all communication of particle positions between the whole processes. Loss of simulation speed by using this method is less than 10% in our simulation, compared with simulations without shear flow.

## 4 Results

### 4.1 Estimation of bending rigidity and surface tension

First, we measured the bending rigidity of the membrane using undulation spectrum analysis and force measurements for implicit-solvent membranes [14, 15]. In the spectrum analysis, undulation spectra of planar strip and cylindrical tube membrane have been calculated to estimate the its bending rigidity. Figure 1 (a) shows a power-spectrum of the height spec-

trum of a tensionless membrane:

$$\langle |h(q)|^2 \rangle = \frac{k_B T}{\kappa q^4}, \quad (7)$$

where  $T$  is the temperature and  $q$  is the wavenumber of the spectrum. Various fitting method for estimation of bending rigidity  $\kappa$  has been attempted in the range  $0 < q < q_{\text{cut}}$  for various cutoff frequencies  $q_{\text{cut}}$ . What is noteworthy in this result is that for various fitting method the estimated bending rigidity provides the same value in the limit of  $q_{\text{cut}} \rightarrow 0$ . At high  $q$  particle protrusion modes  $\langle |h(q)|^2 \rangle \sim q^{-2}$  appears. The influence of the protrusion modes is removed by taking this limit.

Bending rigidity is also estimated by mechanical measurement of cylindrical membrane and buckled membrane. For a cylindrical membrane, it can be estimated using the axial force  $f_z = 2\pi\kappa R^{-1}$  [16]. Figure 1 (b) shows the estimation of  $\kappa$  for  $k_\alpha = 5, 10, 20$  and  $\epsilon = 4$ . When the axial length is not too short,  $\kappa$  can be precisely estimated, in agreement with that calculated using Eq. (7) shown in Fig. 1 (a). Asymmetric membranes have a spontaneous curvature. The spontaneous curvature can be also estimated by this force measurement.

We found that buckled fluid membranes have anisotropic mechanical surface tension [15]. Surprisingly, the surface tension perpendicular to the buckling direction shows stronger dependence on the projected area than that parallel to it. This anisotropy is caused by change of the bending energy as the aspect ratio is varied with a fixed projected area. It can be quantitatively understood by the theoretical analysis of the elastica. The bending rigidity can be also estimated from the area dependence of surface tension.

### 4.2 Aggregation of adhesion sites

First, we investigate interactions between the adhesion sites binding two membranes, and we confirm the conclusions of previous studies [17]. The adhesion sites are distributed

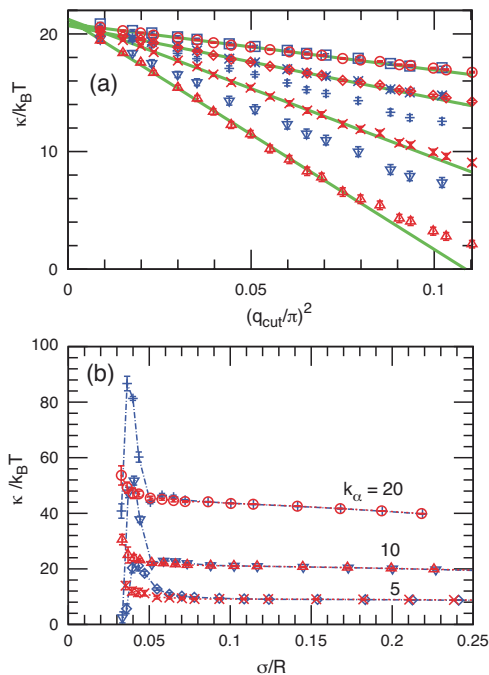


Figure 1: Estimation of the bending rigidity. The data here in is a reprinted from Figs. 3 and 6 of Ref. [14]. (a) Estimated value of the bending rigidity plotted as a function of cutoff frequency of fitting for the implicit-solvent meshless membrane with  $k_\alpha = 5$  and  $\epsilon = 4$ . Different symbols correspond to different fitting method, see Ref. [14] for details. (b) Bending rigidity estimated from axial force measurement of cylindrical membrane, plotted as a function of tube radius  $R$ , for  $k_\alpha = 5, 10, 20$  and  $\epsilon = 4$ .

throughout the membranes and their small clusters are temporally formed but do not grow into large stable clusters [see Fig. 2(a)]. Even if a simulation is started from a large cluster, it gradually dissolves into the mixed state. The cluster size is almost independent of the mean density of adhesion sites.

In order to produce a large stable cluster, the bending entropy of membranes is enhanced by the addition of more layers of membranes [15]. For triple membranes, the adhesion sites form a single large domain, whose shape shows large fluctuations. A few sites often leave the domain but soon return before moving far

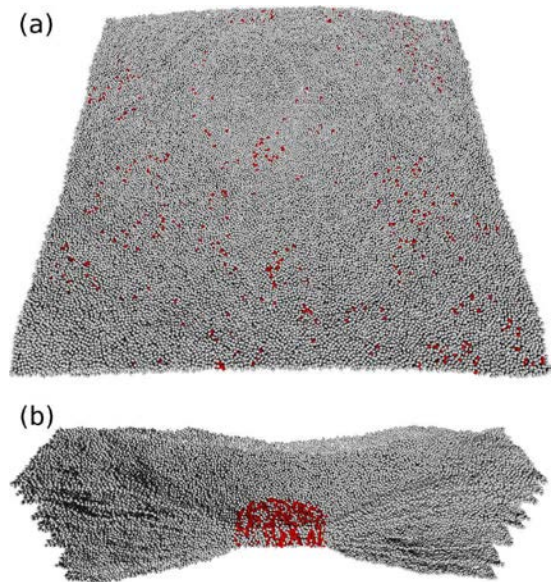


Figure 2: Snapshot of membranes with ligand-receptor adhesion sites. (a) Two membranes are bound. The adhesion sites do not form a large cluster. (b) Eight membranes are bound. The adhesion sites form a circular domain. The front half is removed to show the domain structure. Red (black) and gray spheres represent adhesion sites and membrane particles, respectively.

away, since an isolated site will further suppress the membrane fluctuations of the larger area. With increasing number of the membranes, the domain becomes more compact and circular [see Fig. 2 (b)].

An alternative way to strengthen the entropic force is enhancement of the contribution of each adhesion site [15]. Membrane proteins often modify the structure of surrounding membranes and form an annular shell of specific lipids. Here, we simply consider the effect of the anchor proteins on the main quantity being examined in this study, *i.e.*, bending rigidity. The anchors of ligands or receptors suppress the bending fluctuations of the surrounding membranes. A large stable cluster is successfully formed for a large bending rigidity of the surrounding membranes.

These entropic effects can be understood as

an effective potential in 2D lattice model. Weil and Farago proposed a 2D lattice model to take into account the multibody nature of the interaction [17]. Since local membrane height fluctuations are mainly suppressed by the nearest adhesion site, the entropy of the membrane segment can be expressed by a function of the minimum distance to the nearest site. We have extended their model to take into account multiple membranes and membrane-hardening anchors. Membrane-hardening is treated as a similar interaction to the depletion interaction in the Asakura–Oosaka theory. This simple lattice model reproduces our simulation results very well.

These domain formations are different from those of typical phase separation by a pairwise interaction. When two types of molecules are phase-separated in a binary fluid, a small fraction of either type of molecules dissolves in the other phase. In the case of the membrane adhesion sites, the competition between the entropies in the perpendicular direction (height fluctuations) and in the horizontal directions (mixing of the adhesion sites) determines the phase behavior. While a large amount of unbonded membrane particles dissolves in circular domains, no adhesion sites dissolve in the membranes even from largely deformed domains. This asymmetry is caused by the long-range height correlation of the membranes. Such stable domains involving other lipids and proteins may form a good platform for biological functions.

### 4.3 Membranes with grafted polymers

We investigate the edge line tension with various grafted polymer densities for both ideal chains and excluded-volume chains. A strip of single-phase membrane with grafted polymers is used to estimate the edge tension. The edge tension decreases with increasing polymer density. The reduction for excluded-volume chains is much larger than that for ideal chains. When

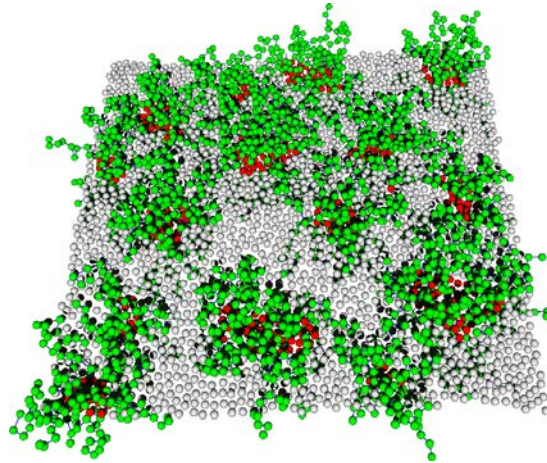


Figure 3: Snapshot of membranes with grafted polymer chains. The membrane consists of two types [red (or dark gray) and light gray] of the membrane particles. The polymer chains are grafted on the (red or dark gray) membrane particles. The polymer grafting induces microdomain formation. Without polymers, a single large domain is formed.

the polymers stay on the membrane edge, they can have more space to move *i.e.* more conformational entropy. We proposed a mean field theory for the edge line tension reduced by grafted ideal chains, which well reproduces our simulation results.

To clarify the polymer effects on the membrane domain, we added grafted polymer into a phase-separated circular domain. As polymer density is increased, the domain shape is fluctuated and subsequently the domain is divided into small domains (see Fig. 3). The line tension between the membrane domains is estimated by two methods using a striped domain and a 2D Laplace pressure of a circular domain. For the membrane without polymer, the obtained values agree with those from the membrane strip very well. However, the values obtained from the Laplace pressure are slightly larger for the polymer-grafted membranes. Thus, more curved domains have lower reduction of the line tension, so that the small domains with a high curvature can have suffi-

ciently large line tension to keep the domain, whereas a large domain is unstable. The entropic effects of glycolipids may play a significant role in stabilizing microdomains  $\lesssim 100$  nm in living cells.

#### 4.4 Concentric structure formation under shear flow

In the absence of shear flow, the membrane structures depend on the membrane volume fraction  $\varphi$ . While at a low volume fraction ( $\varphi = 0.0625$ ), vesicles with around 100 particles appear. Increasing  $\varphi$ , the membrane layer become percolated throughout the system, to form lamellar stack at around  $\varphi = 0.25$ . At a large scale, orientation of these lamellar stacks are not completely aligned, because the relaxation time to the equilibrium state far exceeds the simulation time.

When apply shear flow to this system, the orientation of the lamellar layers formed at high membrane compositions ( $\varphi \geq 0.25$ ) become aligned in a short time. In Fig. 4, the membrane layers are visualized for  $\varphi = 0.3125$ , at a shear rate  $\dot{\gamma}\tau =$  (a)  $2.84 \times 10^{-2}$  and (b)  $14.2 \times 10^{-2}$ . Here,  $\tau$  is a typical time scale of this system that is used as a time unit in our simulation. At a low shear rate (a), lamellar layers are aligned in the direction of shear flow over all the system, accompanying defects inside. At higher shear rates, the lamellar layers exhibits concentric instability *i.e.* formation of rolled-up conformation as shown in Fig.4 (b). The membranes layers are completely aligned with the flow directions, and the instability takes place in the direction perpendicular to the shear velocity. Its structure factors are qualitatively in consistency with the precursor state of the onion formation in the time-resolved scattering experiments.

Figure 5 shows the dynamical phase diagram as a function of membrane composition  $\varphi$  and the shear rate  $\dot{\gamma}$ . At a low shear rate, the system changes from vesicle to aligned lamellar state with increasing  $\varphi$ . At a high membrane

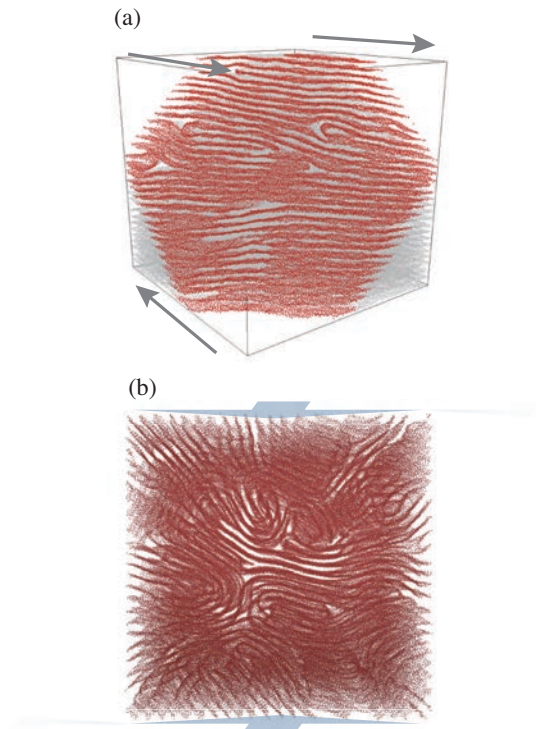


Figure 4: (a) Cross-sectional snapshot in a steady state, at  $\varphi = 0.3125$  and  $\dot{\gamma}\tau = 2.84 \times 10^{-2}$ . This snapshot corresponds to Fig. 7 (a) in Ref. [9]. The arrow indicate the shear flow direction. (b) Snapshot of roll state observed at  $\varphi = 0.2125$  and  $\dot{\gamma}\tau = 14.2 \times 10^{-2}$ . The shear flow is applied in the direction perpendicular direction to the paper. (Reprinted from Ref. [8]. ©2014 The Molecular Simulation Society of Japan)

volume fraction, for example at  $\varphi = 0.25$ , a transition occurs from lamellar state to rolled up state (at  $\dot{\gamma}t = 1.42 \times 10^{-2}$ ), and then enter into lamellar state takes place again. Although the final onion phase has not been obtained at present, the phase diagram has several common characteristics with the experiments [5]. Remarkable resemblance is seen in a reentrant appearance of the lamellar state as a function of shear rate  $\dot{\gamma}$ , at large  $\varphi$  region. Moreover, in the lamellar state at low- $\dot{\gamma}$  defect density seems much higher that at high  $\dot{\gamma}$ , which seems to be in line with the description in Ref. [5]. Thus, our simulation reproduces the a concen-

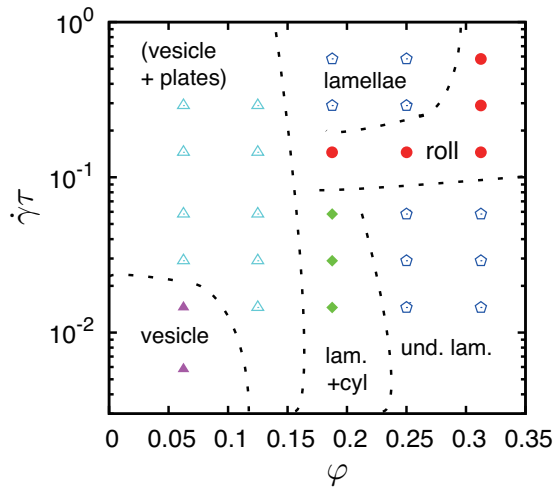


Figure 5: Dynamical phase diagram as a function of the volume fraction  $\varphi$  of the membrane component and the shear rate  $\dot{\gamma}\tau$ . (Reprinted from Ref. [9]. ©2013 AIP Publishing LLC)

tric structure as a precursor of onion formation, and it is likely that this model will reproduce the onion phase if the simulation condition (including the system size) becomes appropriate.

## 5 Summary

We have presented the structure formation of the membrane using meshless membrane simulations. Membranes show a rich variety of behavior in thermal equilibrium as well as out of equilibrium. Coarse graining is a powerful tool to investigate membrane dynamics on a micro meter scale. On this scale, a detailed molecular structure can be neglected. The meshless model is suitable to treat topological changes of membranes. In the shear flow, we have found a novel rolled lamellar structures, which capture the feature of the intermediate scattering pattern during the lamellae-to-onion transition. We will further pursue the onion phase and other large scale phenomena using supercomputers.

## References

- [1] A. -S. Smith, K. Sengupta, S. Goennenwein, U. Seifert, and E. Sackmann, *Proc. Natl. Acad. Sci. USA* **105**, (2008) 6906.
- [2] A. S. Achalkumar, R. J. Bushby, and S. D. Evans, *Soft Matter* **6** (2010) 6036.
- [3] H. Noguchi, *EPL* **102** (2013) 68001.
- [4] H. Wu, H. Shiba, and H. Noguchi, *Soft Matter* **9** (2013) 9907.
- [5] O. Diat, D. Roux, and F. Nallet, *J. Phys. II France* **3** (1993) 1427.
- [6] C.-Y. David Lu, *Phys. Rev. Lett.* **109** (2012) 128304.
- [7] F. Nettesheim, J. Zipfel, U. Olsson, F. Renth, P. Lindner, and W. Richtering, *Langmuir* **19** (2003) 3603.
- [8] H. Shiba and H. Noguchi, *Ensemble (Bulletin of Molecular Simulation Society of Japan)* **16** (2014) 59. [in Japanese]
- [9] H. Shiba, H. Noguchi, and G. Gompper, *J. Chem. Phys.* **139** (2013) 014702.
- [10] H. Noguchi, *J. Phys. Soc. Jpn.* **78**, (2009) 041007.
- [11] H. Guo, K. Kremer, and T. Soddemann, *Phys. Rev. E* **66** (2002) 061503.
- [12] H. Noguchi and G. Gompper, *Phys. Rev. E* **73** (2006) 021903.
- [13] H. Noguchi and G. Gompper, *J. Chem. Phys.* **125** (2006) 164908.
- [14] H. Shiba and H. Noguchi, *Phys Rev. E* **84** (2011) 031926.
- [15] H. Noguchi, *Phys Rev. E* **83** (2011) 061919.
- [16] V. A. Harmandaris and M. Deserno, *J. Chem. Phys.* **125** (2006) 204905.
- [17] N. Weil and O. Farago, *Euro. Phys. J. E* **33** (2010) 81.